Signal-to-Noise Ratio Analysis Based on Different Space Remote Sensing Instruments

Lei Zhang, Bo Li, Hanshuang Li, Guochao Gu, and Xiaoxu Wang

***Abstract*— Signal-to-noise ratio (SNR) analysis is a crucial component of optical system development for space remote sensing instruments. It serves as a quantitative assessment of the imaging quality and radiometric characteristics of space remote sensing. This paper utilizes the working principles and energy transfer principles of space remote sensing instruments to conduct SNR analysis and model development for commonly used spaceborne imagers, spaceborne imaging spectrometers, micro-optical remote sensing instruments, and point-source spatial targets. Additionally, the paper also examines the impact of the presence and width of slits in different space environments on the SNR of space remote sensing instruments. The calculation results indicate that the analysis of Signal-to-Noise Ratio (SNR) for different space remote sensing instruments requires the establishment of distinct SNR models. The magnitude of SNR primarily depends on crucial factors such as optical system quality, detector performance, and the space environment. Therefore, in the instrument design and data processing processes, it is essential to consider how to maximize SNR and establish more accurate corresponding SNR models to provide high-quality remote sensing data.**

***Index Terms*—Detector, energy transfer, signal-to-noise ratio, space remote sensing.**

I. Introduction

SPACE remote sensing instruments enable real-time or periodic observation of various phenomena and changes on Earth's surface on a global scale. This includes natural disasters, climate change, land use, vegetation dynamics, ocean dynamics, water resource conditions, and more [1], [2], [3], [4], [5]. They are instrumental in providing scientists with timely access to extensive Earth observation data, facilitating the monitoring of environmental changes and early warning of potential risks. Space remote sensing instruments not only play an important role in earth observation, but also hold significant importance in space exploration and cosmic research. They can be used to observe planets, stars, galaxies, and other celestial bodies, helping to unravel the mysteries of the universe and advancing our understanding of the cosmos [6], [7], [8], [9], [10], [11]. Due to their capability to simultaneously capture two-dimensional or three-dimensional spatial information along with spectral information of targets, space remote sensing instruments provide powerful data resources that have a profoundly significant impact on the development of remote sensing science and modern scientific and technological applications.

Signal-to-Noise Ratio (SNR) is a critical metric for describing the ability of space remote sensing instruments to acquire relevant target information. Its magnitude reflects the instrument's detection capability for targets and directly impacts inversion calculations. In remote sensing images, we often need to detect and identify targets such as buildings, vegetation, water bodies, etc. [12], [13], [14]. Space remote sensing instruments perform inversion calculations by utilizing energy information from various spectral bands, allowing us to obtain surface information within target areas. This information plays a crucial role in applications like natural disaster early warning and ecological environment monitoring.

SNR directly affects the quality of remote sensing images. A higher SNR implies a relatively strong signal and lower background noise. During the imaging process, a higher ratio of signal to noise leads to better image quality, making details and features more clearly visible. Images with a high SNR facilitate more accurate extraction and interpretation of surface information and support subsequent remote sensing applications and analyses [15], [16], [17]. At the same time, in the data processing and information extraction process of remote sensing images, SNR affects data reliability and accuracy. Noise interference can lead to data errors and uncertainties, and images with high SNR can reduce this impact and improve data reliability. Therefore, correctly estimating the proportion of effective energy information in the optical field of space remote sensing instruments is a prerequisite for achieving high-precision inversion algorithms.

Properly assessing and calculating SNR is a crucial challenge for designers of space remote sensing instruments [17], [18], [19]. Different types of space remote sensing instruments for various purposes require different SNR calculation methods, necessitating classification and accurate establishment of SNR models for each of them.

II. SNR Analysis Model

SNR is a crucial metric for measuring the radiometric sensitivity of space remote sensing instruments. The magnitude of noise

Manuscript received 27 September 2023; revised 30 October 2023; accepted 2 November 2023. Date of publication 6 November 2023; date of current version 8 April 2024. This work was supported in part by the National Natural Science Foundation of China under Grant 62205330 and in part by the Strategic Priority Research Program of the Chinese Academy of Sciences under Grant XDA28050102. *(Corresponding author: Bo Li.)*

Lei Zhang is with the Changchun Institute of Optics, Fine Mechanics and Physics, Chinese Academy of Sciences, Changchun, Jilin 130033, China, and also with the University of Chinese Academy of Sciences, Beijing 100049, China (e-mail: zhanglei990814@163.com).

Bo Li, Hanshuang Li, Guochao Gu, and Xiaoxu Wang are with the Changchun Institute of Optics, Fine Mechanics and Physics, Chinese Academy of Sciences, Changchun, Jilin 130033, China (e-mail: libo01@ciomp.ac.cn; 31397256@qq.com; guguochao@ciomp.ac.cn; wangxiaoxu@ciomp.ac.cn).

Digital Object Identifier 10.1109/JPHOT.2023.3330391

determines the accuracy achievable in identifying target spectral features. In situations where the target radiation is low and the signal is weak to the extent that it is drowned out by noise, even instruments with high resolution cannot produce high-quality images. In order to analyze the SNR of space remote sensing instruments, this paper employs the equivalent electron method to establish models for signal electron count and noise electron count. This approach quantifies electron counts as the unit for signal and noise standard deviations. The ratio of the sum of signal electron counts and various noise electron counts received by the detector defines SNR:

$$SNR = \frac{N_{signal}}{N_{noise}} \tag{1}$$

Where N_{signal} and N_{signal} represent the signal electron count and the noise electron count, respectively. So it is necessary to establish detailed computational and analytical models for both the signal electron count and the noise electron count.

To begin with, it is essential to establish a radiance model at the entrance pupil of the space remote sensing instrument. We employ the widely used atmospheric transmission simulation software MODTRAN for prior simulations in advance. This allows us to obtain spectral radiance data at the entrance pupil of the space remote sensing instrument under various conditions, including sun or moon illumination, different atmospheric conditions, varying sun zenith angles, and different ground surface reflectances [20]. By combining these data with the optical system's parameters, we convert the entrance pupil radiance into spectral radiative flux received at the detector's focal plane. Once the radiative signal enters the detector, it needs to be transformed into the number of photo-generated electrons in the detector, taking into account the detector's quantum efficiency. This completes the model for the number of signal electrons. The noise model primarily depends on the type and performance of the detector, and the following sections will provide noise analyses for detectors of different application types.

A. Signal Electron Count Analysis Model

Signal light passes through the atmosphere and reflected by the ground target before reaching the entrance pupil of the space remote sensing instrument's optical system. Therefore, when the light source is fixed, the radiation received at the entrance pupil primarily depends on the atmospheric transmittance in different space environments conditions, the reflectance of ground targets with respect to the signal light and the detection distance. The radiative flux received at the entrance pupil undergoes photoelectric conversion in the optical system [21], incurring some energy loss. which contains a certain amount of energy loss. Therefore, considering the detector's quantum efficiency, the count of signal electrons generated by the detector can be determined by (2):

$$S = \int_{\lambda_1}^{\lambda_2} \frac{E(\lambda)}{h \cdot c/\lambda} \cdot A \cdot \eta \cdot t d\lambda \tag{2}$$

Where, S represents the number of signal electrons received on the imaging detector, $E(\lambda)$ is the radiance at the focal plane, h is the Planck constant, c is the speed of light in vacuum, A is the pixel area, η is the average quantum efficiency of the detector, and t is the integration time of the detector. It can be observed that the number of signal electrons is directly proportional to the irradiance at the focal plane of the detector, the pixel area and the integration time.

B. Noise Electron Count Analysis Model

During the process of radiative transmission and photoelectric conversion in space remote sensing instruments, they inevitably encounter interference from both external environmental factors and internal instrument characteristics, collectively referred to as noise. Detector noise constitutes the primary source of noise in space remote sensing instruments, primarily including photon shot noise (σ_{shot}), dark current noise (σ_{dark}) and readout noise (σ_{read}).

Photon shot noise is noise related with random changes in the number of incident photons [22]. The optical signals enter the system and being detected can be considered as a random and independent process for each photon. Therefore, the root mean square value of shot noise is given by (3):

$$\sigma_{shot} = \sqrt{N_{signal}} = \sqrt{S} \tag{3}$$

Dark current noise is electronic noise caused by dark current and is related to the magnitude and variation of the dark current. It is typically represented as the standard deviation of the dark current [23], [24], [25]. Dark current refers to the amount of current released by a photodiode when there is no incident light. Ideally, dark current should be zero, but in reality, each pixel's photodiode also acts as a capacitor. Even in the absence of incident light, as the capacitor slowly releases charge, the dark current voltage can be equivalent to the output voltage of low-luminance incident light. Dark current depends on operating temperature and integration time, and cooling the detector can significantly reduce the intensity of dark current.

After the detector is exposed to light, it generates free electrons or holes in potential wells. The stronger the light intensity, the more electric charge is generated. When extracting the signal, it's necessary to transfer the charge in an orderly manner. Therefore, the transfer of charge within pixels must occur in a specific direction. As accumulated charge moves on the detector, electrons may jump forward or backward, resulting in noise known as readout noise [26], [27]. Readout noise is related to the speed of readout charge and is independent of integration time.

In order to maintain unit consistency with the signal, electron count is also used as the unit of measurement when calculating noise. Assuming that various noise source are independent, the total random noise electron count can be expressed by (4):

$$\sigma = \sqrt{\sigma_{shot}^2 + \sigma_{dark}^2 + \sigma_{read}^2} = \sqrt{S + n_{dark} + \sigma_{read}^2} \tag{4}$$

Where n_{dark} represents the detector's dark current. Therefore, the SNR model of space remote sensing instruments can be established as follows:

$$SNR = \frac{S}{\sigma} = \frac{\int_{\lambda_1}^{\lambda_2} \frac{E(\lambda)}{h \cdot c/\lambda} \cdot A \cdot \eta \cdot t d\lambda}{\sqrt{\mathrm{S} + \mathrm{n_{dark}} + \sigma_{\mathrm{read}}^2}} \tag{5}$$

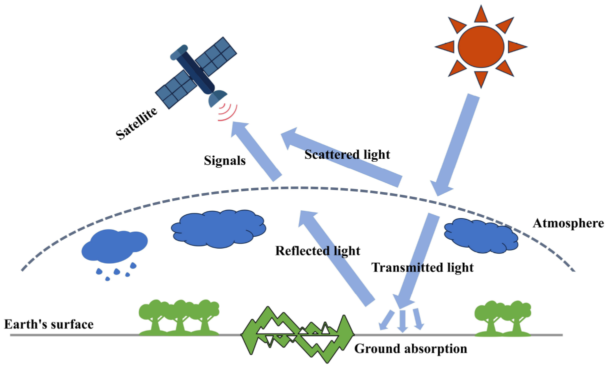

Fig. 1. Optical signal transmission model.

III. SNR Analysis for Spaceborne Imagers and Spaceborne Imaging Spectrometers

The SNR model can effectively reflect the sensitivity of space remote sensing instruments. However, during the actual operation of satellites in orbit, the quality of Earth remote sensing information acquired by space remote sensing instruments is constrained by various factors. These factors mainly include the type of remote sensing instrument, optical system technical specifications, and lighting conditions, among others. As shown in Fig. 1, the signal radiation emitted by the light source will be scattered and absorbed by the Earth's atmosphere and surface during the transmission process. This can result in some differences between the images received by the detector and the actual surface information. Below, we will establish and analyze the SNR model for spaceborne imager and spaceborne imaging spectrometer.

A. SNR Analysis of Spaceborne Imager

Space-based space target monitoring technology has become a cutting-edge technology in today's space exploration field. Spaceborne imagers as a crucial component of space-based space target monitoring systems, enable the identification and tracking of critical space targets. Simultaneously, they provide essential characteristics of space targets, such as shape, size, and orbital altitude [28], [29], [30], [31]. This technology represents an important direction for the future development of space situational awareness. SNR is one of the key indicators for space remote sensing optical payloads and plays a crucial role in determining whether accurate target recognition and high-resolution remote sensing imagery can be obtained.

To establish the SNR analysis model for the spaceborne imager based on its operational mode, orbit characteristics, and detector performance, we first used MODTRAN software to simulate the radiance values received at the entrance pupil of the imaging camera when a certain Earth observation satellite is in orbit. The specific simulation parameters are shown in Table I. Fig. 2 shows the radiance value curve received at the entrance pupil of the spaceborne imager in the wavelength range of 400 to 800 nm after the MODTRAN simulation. The horizontal coordinate represents the wavelength, the vertical coordinate represents the radiance value, and the solid line represents the radiance value received at the entrance pupil of the spaceborne imager.

TABLE I
Simulation Parameters of Modtran

Parameters	Value
Atmospheric model	Mid-latitude summer
Type of Atmospheric path	Slant path
Aerosol Model	Rural-VIS=23km
Observer height	400km
Final height	0km
Initial wavelength	400nm
Final wavelength	800nm
Temperature at first boundary	300K
Zenith Angle	180°
Sun zenith angle	30°
Surface Albedo	0.3

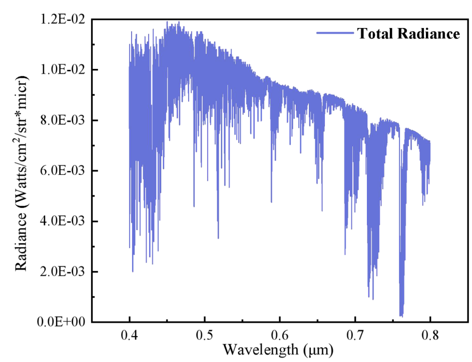

Fig. 2. Radiance simulation at the entrance pupil of the spaceborne imager.

TABLE II
Main Parameters of Spaceborne Imager

Parameters	Value
Spectral range	400~800nm
Entrance pupil	20mm
Field	10°
Focal length	100mm
$F^{\#}$	5
Spectral radiative transfer efficiency	0.7
Integration time	1ms

Using the prototype of this spaceborne imager as an example, we will proceed with the calculation of the SNR model. The main optical system parameters are showed in Table II.

Based on the energy transfer and loss principle to analyze the SNR model of the spaceborne imager. When the operational altitude of the spaceborne imager is H, the solid angle of the ground acquisition target to the spaceborne imager is:

$$\Omega = \frac{dS}{H^2} = \frac{\pi \cdot D_r^2}{4H^2} \tag{6}$$

Where H is the orbit altitude. D_r is the swath width, which is the diameter of the ground acquisition target:

$$D_r = 2H \cdot tan\,(\theta/2) \tag{7}$$

Where θ is the instantaneous field of the spaceborne imager. The spaceborne imager uses the ground target as the surface extended source for vertical sampling. The entrance pupil of the imager acts as the illuminated surface. According to the principle of radiance-to-irradiance conversion, the irradiance $E_v(\lambda)$ at the entrance pupil of the spaceborne imager is:

$$E_v(\lambda) = \Omega \cdot L(\lambda) = \frac{\pi \cdot {D_r}^2 \cdot L(\lambda)}{4H^2} \tag{8}$$

From the energy distribution, it can be seen that under uniform illuminance, all the energy received at the entrance pupil is eventually evenly distributed across each pixel of the detector after passing through the optical system. Using this approach, we can calculate the total energy reaching the entrance pupil and the resulting image size on the focal plane. This allows for the determination of the energy density for each pixel on the detector. Finally, we can compare the number of signal electrons received by an individual pixel during the integration time with the corresponding output noise electrons to establish the SNR model for the spaceborne imager. The method for calculating the number of signal electrons is as follows:

$$S = \int_{\lambda_1}^{\lambda_2} \frac{E\,(\lambda) \cdot D^2 \cdot A_0 \cdot T \cdot \eta \cdot t}{h \cdot c/\lambda \cdot d^2} d\lambda \tag{9}$$

Where D is the diameter of entrance pupil of the spaceborne imager, A_0 is the area of a single pixel. And d is the diameter of the linear field of view, which can be determined by the following formula:

$$d = 2f' \cdot tan\,(\theta/2) \tag{10}$$

Where f' is the focal length of the optical system of the spaceborne imager.

Finally, the number of signal electrons received by a single pixel in this model can be expressed as:

$$S = \int_{\lambda_1}^{\lambda_2} \frac{\pi}{4(F\#)^2} \cdot \frac{L\,(\lambda) \cdot A_0 \cdot T \cdot \eta \cdot t}{h \cdot c/\lambda} d\lambda \tag{11}$$

Since the imager does not possess spectral separation capabilities, each pixel receives a full-band spectral signal.

By substituting the optical system parameters from Table II into (11), the number of signal electrons received by a single pixel, S, is calculated to be 50482. At this time, it is necessary to initially verify the calculation by comparing it to the full well charge of the detector. The number of signal electrons received by a single pixel should to be less than the full well charge of the detector.

Similarly, as shown in Fig. 3, the focal plane irradiance of the spaceborne imager can be expressed in terms of the entrance pupil radiance and optical system parameters of the spaceborne imager:

$$E\,(\lambda) = \frac{L\,(\lambda) \cdot T \cdot S_D}{f'^2} = \frac{\pi}{4} L\,(\lambda) \cdot T \cdot \left(F^{\#}\right)^{-2} \tag{12}$$

Where A is the entrance pupil area of the imager, and (12) indicates that the image plane irradiance of the imager is directly proportional to the square of the relative aperture, meaning that the SNR of the spaceborne imager is inversely proportional to the $F^{\#}$ of the optical system.

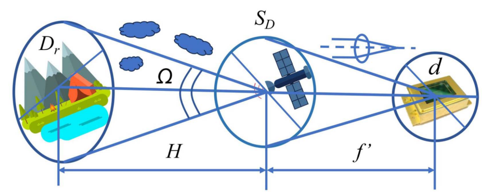

Fig. 3. Irradiance of a surface light source on an illuminated surface.

TABLE III
MAIN PARAMETERS OF THE DETECTOR

Parameters	Value
Pixel size	9μm
Number of pixel	4096×4096
Average quantum efficiency	0.7
Full well charge	74ke-
Readout noise	3.7e-
Dark current noise	12.2e-/p/s

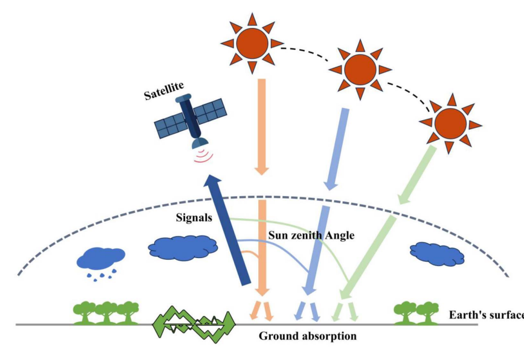

Fig. 4. Schematic of different sun zenith angle.

After obtaining the signal electron count model of the spaceborne imager, it is necessary to analyze the noise signals of the imager. The main parameters of the detector are shown in Table III.

By substituting the above detector parameters and signal electron count into the noise signal model (4), the noise electron count of the spaceborne imager can be calculated as (13):

$$\sigma = \sqrt{\mathrm{S} + \mathrm{n_{dark}} + \sigma_{\mathrm{read}}^2} = 224.7 \tag{13}$$

Finally, the SNR value for the spaceborne imager in this model is 225.

Summarizing, the SNR analysis model of the spaceborne imager can be represented by (14). This shows that the SNR of space remote sensing instrument is affected by many factors, including space environment, optical system performance parameters, detector parameters and exposure time of the instrument. For the same spaceborne imager, different space environmental conditions will also significantly affect the SNR. Figs. 4 and 5 respectively show schematic illustrations of observations at different sun zenith angles and the magnitude of the radiance

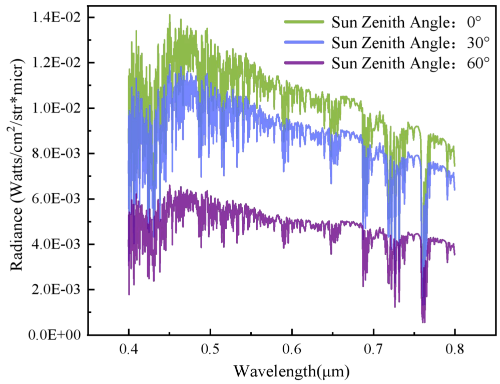

Fig. 5. Entry pupil radiance at different sun zenith angles.

at the entrance pupil of the space remote sensing instrument.

$$SNR = \frac{S}{\sigma} = \frac{\int_{\lambda_1}^{\lambda_2} \frac{\pi}{4(F\#)^2} \cdot \frac{L(\lambda)\cdot A_0\cdot T\cdot \eta\cdot t}{h\cdot c/\lambda} d\lambda}{\sqrt{\mathrm{S} + \mathrm{n_{dark}} + \sigma_{\mathrm{read}}^2}} \tag{14}$$

B. SNR Analysis of Imaging Spectrometer

Imaging spectrometers are highly efficient quantitative detection instrument that can capture continuous monochromatic spectral images of the target or scene of interest. They construct a three-dimensional observation data cube by combining spatial and spectral data dimensions. This provides researchers with detailed spatial and spectral characteristics for every point within the target or scene [32], [33], [34]. This combination of high-resolution imaging capabilities similar to a camera and high spectral resolution capabilities like a spectrometer makes imaging spectrometers widely applicable in tasks such as remote sensing for mapping, target identification, environmental monitoring and assessment, clinical image diagnosis, process monitoring, and more. They play a significant role in various fields including geography, space, oceanography, climate science, atmospheric studies, agriculture, vegetation analysis, ecology, medicine, security, manufacturing, and colorimetry, among others [35], [36], [37], [38], [39].

It is assumed that the working mode of the dispersive imaging spectrometer and the detector used are the same as the imager mentioned in Section III-A, but due to the addition of a subsequent spectrometer system, the spectral transmission efficiency has been slightly reduced, and we also need to consider the diffraction efficiency of the grating component, the updates to Table IV are as follows.

From the analysis in Section III-A, it can be determined that the spectral irradiance ultimately incident on the focal plane of the imaging spectrometer is:

$$E(\lambda) = \frac{\pi}{4} L(\lambda) \cdot T \cdot T_g \cdot \left(F^{\#}\right)^{-2} \tag{15}$$

The number of signal electrons ultimately received on the detector can be expressed as:

$$S = \int_{\lambda_1}^{\lambda_2} \frac{E(\lambda) \cdot A \cdot \eta \cdot t}{h \cdot c/\lambda} d\lambda \tag{16}$$

TABLE IV
MAIN PARAMETERS OF SPACEBORNE IMAGING SPECTROMETER

Parameters	Value
Spectral range	400~800nm
Entrance pupil	20mm
Field	10°
Focal length	100mm
$F^{\#}$	5
Spectral radiative transfer efficiency	0.6
Diffraction efficiency of grating	0.6
Spectral resolution	1nm
Spectral sampling interval	0.5nm
Integration time	1s
Slit width	9μm

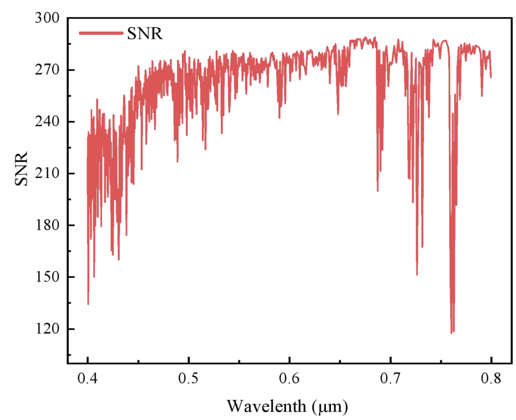

Fig. 6. SNR in various spectral bands of imaging spectrometer.

For the detector of the imaging spectrometer, the operating band $\Delta\lambda$ corresponding to each pixel is very narrow, so there is no need to integrate. Therefore, (12) can be written as:

$$S_p = \int_{\lambda}^{\lambda+\Delta\lambda} \frac{E(\lambda) \cdot A_0 \cdot \eta \cdot t}{h \cdot c/\lambda} d\lambda = \frac{E(\lambda) \cdot A_0 \cdot \eta \cdot t}{h \cdot c/\lambda} \cdot \Delta\lambda \tag{17}$$

The SNR model for the spaceborne imaging spectrometer can be represented by comparing the signal electron count obtained using (17) with the noise electron count calculated using (4). The SNR values corresponding to each spectrum can be obtained as shown in Fig. 6. Fig. 7 shows the impact of different solar zenith angles on the SNR of the imaging spectrometer.

During the actual operation of the spaceborne spectrometer, the presence of a slit results in a significant portion of the energy not being able to enter the spectrometer system it is docked with. Below, we will analyze the SNR model of the imaging spectrometer using the principle of energy transmission.

The energy received by the spaceborne imaging spectrometer is focused onto the image plane of the telescope system, where the slit coincides with the image plane. At this point, the energy of various wavelengths at the location of the slit Q_s is:

$$Q_s = E(\lambda) \cdot S_d \cdot t \cdot \lambda \tag{18}$$

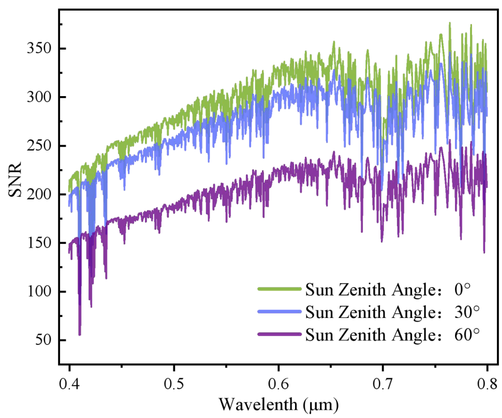

Fig. 7. SNR of imaging spectrometers at different sun zenith angles.

Where S_d is the slit area, which can be expressed as follwos:

$$S_d = d_s \cdot l \tag{19}$$

d_s represents the slit width, which, due to the spectrometer's lack of spatial dispersion, is also the linear field of view diameter. l represents the slit length. Since the spectral resolution is 1 nm, and the spectral sampling interval is 0.5 nm, this means that a single wavelength will ultimately occupy the size of two pixels on the detector's image plane. This implies that the width of the slit is theoretically equal to the size of a single pixel occupied by spectral sampling.

The irradiance $E_s(\lambda)$ at the slit can be represented as follows:

$$E_s(\lambda) = \frac{\pi}{4} L(\lambda) \cdot T \cdot \left(F^{\#}\right)^{-2} \tag{20}$$

The energy of a single wavelength, after dispersion through the spectrometer system, is distributed across two pixels on the detector focal plane in the spectral dimension. The energy received by a single pixel can be represented as:

$$Q_i = \frac{Q_s \cdot T_g \cdot \eta}{d.l_i} \cdot A = E(\lambda) \cdot A_0 \cdot \eta \cdot t \cdot \Delta\lambda \tag{21}$$

Ultimately, the number of signal electrons on a single pixel is similarly calculated by dividing the total energy received by the energy of a single photon. It is worth noting that this SNR model is the same as the calculated results of (13). When analyzing the SNR model of a spaceborne imaging spectrometer in practice, a more accurate method is to consider the width of the slit.

When we widen the width of the slit, the corresponding SNR will also increase. Fig. 8 shows the SNR of the imaging spectrometer after doubling the slit width. From the figure, it can be seen that increasing the slit width can enhance the SNR, but it will also reduce the spectral sampling interval. Therefore, in practical applications, it is necessary to consider the SNR index and resolution of the optical system comprehensively to find a balance between the two.

IV. SNR Model of Microlight Remote Sensing Instrument

The study of microlight imaging technology is a technique for optical image acquisition, enhancement, processing, transmission, storage and display in low illumination environment [40],

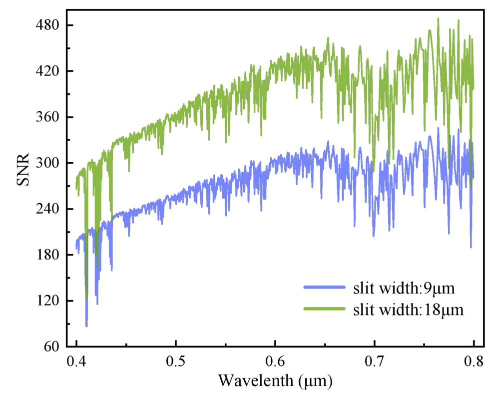

Fig. 8. Effect of slit width on SNR of imaging spectrometer.

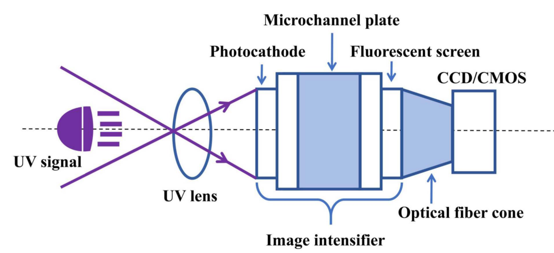

Fig. 9. Image intensifier schematic.

[41], [42]. Due to the limitations of the human eye, which restricts the ability of human beings to capture images at night, the microlight night vision technology enhances the visual perception of the human eye at night. Additionally, because ultraviolet radiation is heavily absorbed by the atmosphere, conventional imaging techniques struggle to utilize the ultraviolet spectral range for spectral analysis. Image intensifier can effectively compensate for this deficiency, which is of great significance in both military and civilian applications.

With the continuous development of solid-state imaging devices such as CCD and CMOS, the integration of image intensifiers with CCD/CMOS, known as ICCD and ICMOS technologies, is rapidly developing and finding widespread applications in various fields. This technology is the mainstream choice for microphoto detectors. For space remote sensing instruments using image intensifier, it is also necessary to separately establish models for the signal electron count and the noise signal electron count. The signal electron count, amplified after being received by the detector's focal plane, can be represented as follows:

$$S = G \cdot \int_{\lambda_1}^{\lambda_2} \frac{E(\lambda)}{h \cdot c/\lambda} \cdot A \cdot \eta \cdot t d\lambda \tag{22}$$

Where G is the total electronic gain multiple of the system.

For microphoto remote sensing imaging, the main source of noise come from the microphoto detectors, including the image intensifier and solid-state imaging devices. Due to the different gain principles of various microphoto detectors, their noise characteristics also differ. The enhanced ICCD/ICMOS devices, while amplifying the effective signal, also amplify noise. The total shot noise is N_{shot} given by (23):

$$N_{shot} = G \cdot F \cdot \sqrt{\frac{S}{G}} \tag{23}$$

Where F is the noise factor, generally between 1.3 to 2 for ICCD and EMCCD.

The dark current has a constant pattern in the image, so it can be directly subtracted from the image. Generally, once the readout speed is determined for CCD/CMOS, their readout noise is fixed. For commonly used ICCD and ICMOS, it can be assumed that there is no gain register, so the dark current noise and readout noise do not increase proportionally in the image intensifier. Therefore, for microphoto remote sensing instruments using image intensifiers, the noise signal model can be represented by (24):

$$\begin{aligned} \sigma &= \sqrt{N_{shot}^2 + n_{dark} + \sigma_{read}^2} \\ &= \sqrt{G \cdot F^2 \cdot S + n_{dark} + \sigma_{read}^2} \end{aligned} \tag{24}$$

Space remote sensing instruments that use image intensifier require a specific analysis of the amplification of various types of noise. The main advantage of ICCD is that the noise of the front-end image intensifier is very low. Compared to hundreds or thousands of electronic gains, dark current noise and readout noise can be considered negligible. The most significant factor affecting ICCD's SNR is the shot noise. As a result, the ICCD's SNR is relatively insensitive to temperature variations.

V. Analysis of the SNR of Infrared Detection Systems for Point Targets in Space

Most of the major components in the exhaust plume of aircraft include H_2O, CO, CO_2, etc. The exhaust plumes generated by flying objects have very high temperatures, often reaching several thousand Kelvin. Additionally, these plumes can extend to lengths of 20 to 30 meters [43], [44], [45]. As a result, the infrared radiation emitted by these exhaust plumes constitutes a significant portion of the overall spectral radiation from the target. 2.7μm and 4.3μm are the main absorption peaks corresponding to H_2O and CO_2 respectively, so infrared detection system is commonly used to monitor and continuously track of high-speed targets in near-space such as aircraft and missiles. When the target is at a considerable distance from the detection system, the target's image on the detector array occupies only 1 to 4 pixels and has no distinctive features. Therefore, it is referred to as a spatial point target [46], [47]. When the distance is relatively close, the target can be regarded as an extended area light source to build the SNR model. A schematic diagram of monitoring flying target using infrared detection technology is shown in Fig. 10.

Atmospheric scattering of sunlight is basically concentrated in the wavelength range of 3μm, and because the temperature of atmospheric molecules and aerosols is not high, radiation amount in the wavelength of 5μm is very weak. Atmospheric radiation dispersion to the sun and its own radiation constitute the sky radiation background. The sky radiation background is at its minimum in the 3$\sim$5um wavelength range, so selecting the

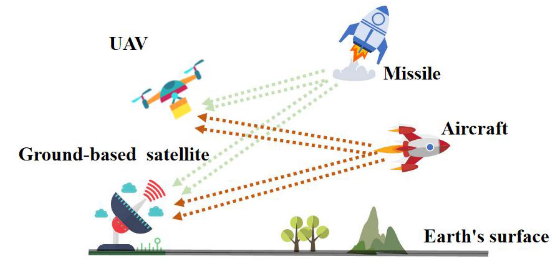

Fig. 10. Schematic of space remote sensing instruments for detecting flying objects.

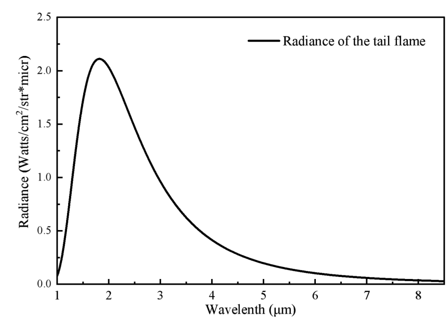

Fig. 11. Simulation results of tail flame radiance.

2$\sim$5um wavelength range as the operational band can reduce the impact of sky background radiation on the detection process.

When the detection device is monitoring or tracking a flight target, the radiation signal of the exhaust plume will be used as a point light source to establish the SNR model of the detection system. After the radiation signal has passed through the atmosphere, it reaches the entrance pupil of the optical system. The radiance at the entrance pupil can be calculated by simulating the radiance of the exhaust plume radiation source and the atmospheric transmittance. Assuming the temperature of the exhaust plume is 2200 K and its emissivity is 0.4, the calculated radiance intensity results are shown in Fig. 11.

Assuming that the airborne detection system and the target are at a distance of R = 5 km, with both the target and the detection system at the same altitude of 6km, the atmospheric model chosen is for mid-latitude summer conditions. Detection of airborne targets is attempted at different zenith angles of 30°, 45°, 60°, and 90°. Fig. 12 shows the schematic diagram of airborne detection system detecting aerial targets at different zenith angles, and Fig. 13 shows the atmospheric transmittance corresponding to different observation angles.

In this case, the entrance pupil irradiance model can be represented as follows:

$$E(\lambda) = \frac{I}{R^2} \tag{25}$$

Formula (25) indicates that when illuminated vertically by a point source, the illuminance $E(\lambda)$ of the illuminated surface is directly proportional to the radiant intensity I of the illuminating source and inversely proportional to the square of the distance from the illuminated surface to the illuminating source. Once the entrance pupil irradiance is determined, the spectral flux and SNR of the point source on the detector focal plane can be

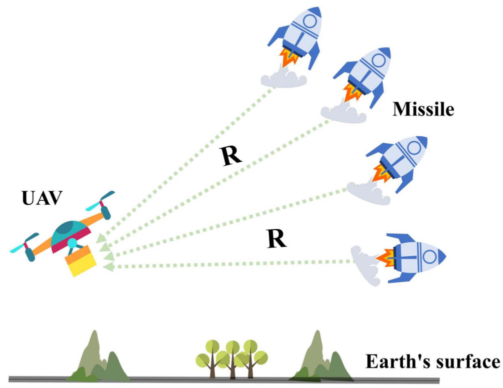

Fig. 12. Detection modes for different zenith angles.

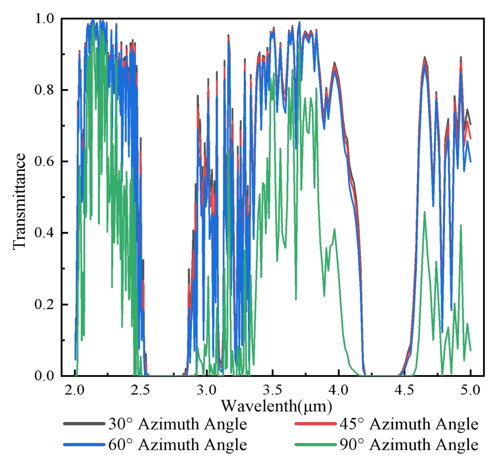

Fig. 13. Transmittance at different zenith angles.

expressed as follows:

$$\emptyset = E(\lambda) \cdot \tau_a \cdot \tau_0 \cdot A = \frac{I \cdot \tau_a \cdot \tau_0 \cdot A}{R^2} \quad (26)$$

$$SNR = \frac{A_0}{R^2\sqrt{A_d \Delta f}} \int_{\lambda_1}^{\lambda_2} I \cdot \tau_a \cdot \tau_0 \cdot D^* d\lambda \quad (27)$$

A_0 and A_d represent the entrance pupil area of the detection system and the pixel size of the detector, Δf is the system noise equivalent bandwidth, and D^* is the spectral detectivity of the detector, which can be found in the detector product manual. Δf and is expressed by (28):

$$\Delta f = \frac{1}{2t} \quad (28)$$

t is the integration time of the detection system. From the above analysis, the process of establishing the SNR model for near space point light source, various factors related to target characteristics, atmospheric properties, and the detection system come into play.

VI. Discussion

The research of SNR models has a broad impact in practical applications, particularly in the fields of signal processing, communications, remote sensing, and experimental design.

In the field of medical imaging, SNR models are widely applied in radiology, magnetic resonance imaging (MRI), ultrasound imaging, computed tomography (CT), and other areas. Researchers use SNR models to optimize imaging parameters, enhance image quality, and reduce radiation doses, all with the aim of improving the accuracy of disease diagnosis.

In the field of remote sensing, SNR models are used to assess the performance of satellite or aircraft sensors. Researchers use these models to select appropriate sensor parameters, such as bandwidth and spectral resolution, to obtain high-quality Earth observation data.

In scientific research, SNR models can be used to determine the sensitivity of experimental design. Researchers can utilize these models to determine the required sample size, experimental parameters, and observation time to ensure the repeatability and reliability of experimental results.

In conclusion, research on SNR models contributes to the optimization and improvement of system performance in various application domains, leading to enhanced data quality, diagnostic accuracy, communication efficiency, and scientific experiment reliability. These models enable researchers to better understand and quantify the relationship between signal and noise, thus better addressing the needs of various application areas. In our future work, there is a need for deeper and introduction of new signal-to-noise ratio measurement methods or applications in specific fields or problems, striving for the most accurate and comprehensive signal-to-noise ratio models possible.

VII. Conclusion

In summary, calculating the SNR of space remote sensing instruments requires a detailed understanding of instrument performance, observation conditions, and the characteristics of both the signal and noise. Appropriate data processing and calculation methods should be employed to ensure accurate signal-to-noise ratio estimation. This article has established SNR models for different types of spaceborne remote sensing instruments, including spaceborne imager, spaceborne imaging spectrometer, microphoto remote sensing instrument using image intensifier and infrared detection system of point light source radiation. It also analyzed the impacts of different calculation methods on the SNR of the optical system. The SNR of space remote sensing instrument is a very important task in the analysis of remote sensing data, because it directly affects the quality and availability of remote sensing data. In a specific application scenario, selecting an appropriate SNR model is crucial for accurately calculating the SNR of a detection system. This choice should take into account the nature of the signal and noise, as well as the background radiation in the current region where the target is located.

References

[1] F. Peri, J. B. Hartley, and J. L. Duda, "The future of instrument technology for space-based remote sensing for NASA's earth science enterprise," in *Proc. Scanning Present Resolving Future. Proc.. IEEE Int. Geosci. Remote Sens. Symp.*, 2001, pp. 432–435, doi: 10.1109/IGARSS.2001.976181.

[2] B. -C. Gao and R. -R. Li, “Removal of thin cirrus scattering effects for remote sensing of ocean color from space,” *IEEE Geosci. Remote Sens. Lett.*, vol. 9, no. 5, pp. 972–976, Sep. 2012, doi: 10.1109/LGRS.2012.2187876.

[3] S. Jin, G. Feng, and S. T. Gleason, “Remote sensing using GNSS signals: Current status and future directions,” *Adv. Space Res.*, vol. 47, pp. 1645–1653, 2011, doi: 10.1016/J.ASR.2011.01.036.

[4] G. Christakos, A. Kolovos, M. L. Serre, and F. Vukovich, “Total ozone mapping by integrating databases from remote sensing instruments and empirical models,” *IEEE Trans. Geosci. Remote Sens.*, vol. 42, no. 5, pp. 991–1008, May 2004, doi: 10.1109/TGRS.2003.822751.

[5] M. George et al., “Carbon monoxide distributions from the IASI/METOP mission: Evaluation with other space-borne remote sensors,” *Atmospheric Chem. Phys.*, vol. 9, pp. 8317–8330, 2009, doi: 10.5194/ACP-9-8317-2009.

[6] K. R. Carver, C. Elachi, and F. T. Ulaby, “Microwave remote sensing from space,” *Proc. IEEE*, vol. 73, no. 6, pp. 970–996, Jun. 1985, doi: 10.1109/PROC.1985.13230.

[7] Y. Wang, Z. Li, G. Lin, and Y. Huang, “High-precision angle prediction of sun for space remote sensing instrument,” *Int. J. Aerosp. Eng.*, vol. 31, pp. 1–9, 2021, doi: 10.1155/2021/8733478.

[8] J. Robinson, “Fire from space : Global fire evaluation using infrared remote sensing,” *Int. J. Remote Sens.*, vol. 12, pp. 3–24, 1991, doi: 10.1080/01431169108929628.

[9] I. Joint and S. B. Groom, “Estimation of phytoplankton production from space: Current status and future potential of satellite remote sensing,” *J. Exp. Mar. Biol. Ecol.*, vol. 250, no. 1-2, pp. 233–255, 2000, doi: 10.1016/S0022-0981(00)00199-4.

[10] R. V. Martin, “Satellite remote sensing of surface air quality,” *Atmospheric Environ.*, vol. 42, pp. 7823–7843, 2008, doi: 10.1016/J.ATMOSENV.2008.07.018.

[11] X. Ye et al., “Instrument development: Chinese radiometric benchmark of reflected solar band based on space cryogenic absolute radiometer,” *Remote Sens.*, vol. 12, 2020, Art. no. 2856, doi: 10.3390/rs12172856.

[12] G. W. D. Vane, A. F. H. Goetz, and J. B. Wellman, “Airborne imaging spectrometer: A new tool for remote sensing,” *IEEE Trans. Geosci. Remote Sens.*, vol. GE-22, no. 6, pp. 546–549, Nov. 1984, doi: 10.1109/TGRS.1984.6499168.

[13] F. Wang, “Improving remote sensing image analysis through fuzzy information representation,” *Photogrammetric Eng. Remote Sens.*, vol. 56, pp. 1163–1169, 1990.

[14] Y. Xie, Z. Sha, and M. Yu, “Remote sensing imagery in vegetation mapping: A review,” *J. Plant Ecol.*, vol. 1, pp. 9–23, 2008, doi: 10.1093/JPE/RTM005.

[15] D. H. Johnson, “Signal-to-noise ratio,” *Scholarpedia*, vol. 1, no. 12, 2006, Art. no. 2088.

[16] Y. Peng, C. Shi, Y. Zhu, M. Gu, and S. Zhuang, “Terahertz spectroscopy in biomedical field: A review on signal-to-noise ratio improvement,” *PhotoniX*, vol. 1, pp. 1–18, 2020, doi: 10.1186/s43074-020-00011-z.

[17] C. Suto, C. Sato, E. Shimamura, H. Toshida, K. Ichikawa, and S. Hori, “Influence of the signal-to-noise ratio on the accuracy of IOLMaster measurements,” *J. Cataract Refractive Surg.*, vol. 33, pp. 2062–2066, 2007, doi: 10.1016/j.jcrs.2007.07.031.

[18] B. Bosworth, W. R. Bernecky, J. D. Nickila, B. Adal, and G. C. Carter, “Estimating signal-to-noise ratio (SNR),” *IEEE J. Ocean. Eng.*, vol. 33, no. 4, pp. 414–418, Oct. 2008, doi: 10.1109/JOE.2008.2001780.

[19] R. Kieser, P. Reynisson, and T. J. Mulligan, “Definition of signal-to-noise ratio and its critical role in split-beam measurements,” *ICES J. Mar. Sci.*, vol. 62, no. 1, pp. 123–130, 2005, doi: 10.1016/J.ICESJMS.2004.09.006.

[20] G. Thuillier, P. Zhu, M. Snow, P. Zhang, and X. Ye, “Characteristics of solar-irradiance spectra from measurements, modeling, and theoretical approach,” *Light, Sci. Appl.*, vol. 11, pp. 56–72, 2022, doi: 10.1038/s41377-022-00750-7.

[21] J. B. Pendry, “Theory of photoemission,” *Surf. Sci.*, vol. 57, pp. 679–705, 1976, doi: org/10.1016/0039-6028(76)90355-1.

[22] Y. M. Blanter and M. Büttiker, “Shot noise in mesoscopic conductors,” *Phys. Rep.*, vol. 336, pp. 1–166, 1999, doi: 10.1016/S0370-1573(99)00123-4.

[23] J. Kublitski et al., “Reverse dark current in organic photodetectors and the major role of traps as source of noise,” *Nature Commun.*, vol. 12, 2021, Art. no. 551, doi: 10.1038/s41467-020-20856-z.

[24] A. Mahmoodi, H. D. Jahromi, and M. H. Sheikhi, “Dark current modeling and noise analysis in quantum dot infrared photodetectors,” *IEEE Sensors J.*, vol. 15, no. 10, pp. 5504–5509, Oct. 2015, doi: 10.1109/JSEN.2015.2443014.

[25] B. Pain, T. Cunningham, B. Hancock, C. Wrigley, and C. Sun, “Excess noise and dark current mechanisms in CMOS imagers,” in *Proc. IEEE Workshop CCD’s Adv. Image Sensors*, 2005, pp. 145–148.

[26] A. Boukhayma, A. Peizerat, and C. C. Enz, “Temporal readout noise analysis and reduction techniques for low-light CMOS image sensors,” *IEEE Trans. Electron Devices*, vol. 63, no. 1, pp. 72–78, Jan. 2016, doi: 10.1109/TED.2015.2434799.

[27] C. Lotto, P. Seitz, and T. Baechler, “A sub-electron readout noise CMOS image sensor with pixel-level open-loop voltage amplification,” in *Proc. IEEE Int. Solid-State Circuits Conf.*, 2011, pp. 402–404, doi: 10.1109/ISSCC.2011.5746370.

[28] J. Nieke, H. Schwarzer, A. Neumann, and G. Zimmermann, “Imaging spaceborne and airborne sensor systems in the beginning of the next century,” *Remote Sens.*, vol. 3221, pp. 581–592, 1997, doi: 10.1117/12.298124.

[29] S. Mindel, “Role of imager in developing world,” *Lancet*, vol. 350, pp. 426–429, 1997, doi: 10.1016/S0140-6736(97)03340-0.

[30] C. J. Willott et al., “The near-infrared imager and slitless spectrograph for the James Webb Space Telescope. II. Wide field slitless spectroscopy,” *Pub. Astronomical Soc. Pacific*, vol. 134, 2022, Art. no. 075001, doi: 10.1088/1538-3873/ac5158.

[31] M. A. Warren et al., “Assessment of atmospheric correction algorithms for the sentinel-2A MultiSpectral imager over coastal and inland waters,” *Remote Sens. Environ.*, vol. 225, pp. 267–289, 2019, doi: 10.1016/J.RSE.2019.03.018.

[32] P. Mouroulis and R. O. Green, “Review of high fidelity imaging spectrometer design for remote sensing,” *Proc. SPIE*, vol. 57, 2018, Art. no. 040901, doi: 10.1117/1.OE.57.4.040901.

[33] D. H. Lumb et al., “Recent developments for the AXAF CCD imaging spectrometer,” *Opt. Photon.*, vol. 57, 1993, Art. no. 1, doi: 10.1117/12.162839.

[34] M. W. Kudenov and E. L. Dereniak, “Compact real-time birefringent imaging spectrometer,” *Opt. Exp.*, vol. 20, no. 16, pp. 17973–17986, 2012, doi: 10.1364/OE.20.017973.

[35] Y. Baikun, “A review of mineral spectral identification methods and models with imaging spectrometer,” *Remote Sens. Land Resour.*, vol. 57, 2007, Art. no. 1.

[36] H. J. Gons, M. Rijkeboer, and K. G. Ruddick, “A chlorophyll-retrieval algorithm for satellite imagery (medium resolution imaging spectrometer) of inland and coastal waters,” *J. Plankton Res.*, vol. 24, pp. 947–951, 2002, doi: 10.1093/PLANKT/24.9.947.

[37] M. Schlerf, C. Atzberger, and J. Hill, “Remote sensing of forest biophysical variables using HyMap imaging spectrometer data,” *Remote Sens. Environ.*, vol. 95, pp. 177–194, 2005, doi: 10.1016/J.RSE.2004.12.016.

[38] J. M. Lerner, “Imaging spectrometer fundamentals for researchers in the biosciences—A tutorial,” *Cytometry Part A*, vol. 69A, pp. 712–734, 2006, doi: 10.1002/cyto.a.20242.

[39] L. Yu, “Development and application of imaging spectrometer (invited),” *Infrared Laser Eng.*, vol. 51, no. 1, 2022, Art. no. 20210940, doi: 10.3788/IRLA20210940.

[40] W. Kim, “Low-light image enhancement: A comparative review and prospects,” *IEEE Access*, vol. 10, pp. 84535–84557, 2022, doi: 10.1109/access.2022.3197629.

[41] X. Zhang, P. Shen, L. Luo, L. Zhang, and J. Song, “Enhancement and noise reduction of very low light level images,” in *Proc. 21st Int. Conf. Pattern Recognit.*, 2012, pp. 2034–2037.

[42] M. Lampton, “The microchannel image intensifier,” *Sci. Amer.*, vol. 245, pp. 62–71, 1981, doi: 10.1038/SCIENTIFICAMERICAN1181-62.

[43] V. N. Kurdyumov and M. Matalon, “Stabilization and onset of oscillation of an edge-flame in the near-wake of a fuel injector,” *Proc. Combustion Inst.*, vol. 31, pp. 909–917, 2007, doi: 10.1016/J.PROCI.2006.07.248.

[44] Y. Chen, F. Huo, and L. Q. Zheng, “Solar-blind ultraviolet optical system design for missile warning,” in *Proc. SPIE*, vol. 9521, 2015, Art. no. 95210X, doi: 10.1117/12.2175626.

[45] L. Lu, W. Sheng, W. Jiang, and F. Jiang, “Research on capability of detecting ballistic missile by near space infrared system,” in *Proc. SPIE*, vol. 10620, 2018, Art. no. 106201T, doi: 10.1117/12.2296416.

[46] B. Zhao, S. Xiao, H.-Z. Lu, and D. Wu, “Spatial-temporal local contrast for moving point target detection in space-based infrared imaging system,” *Infrared Phys. Technol.*, vol. 95, pp. 53–60, 2018, doi: 10.1016/J.INFRARED.2018.10.011.

[47] Y. Xi et al., “Infrared moving small target detection based on spatial-temporal local contrast under slow-moving cloud background,” *Infrared Phys. Technol.*, vol. 134, 2023, Art. no. 104877, doi: 10.1016/j.infrared.2023.104877.